https://doi.org/10.1038/s41586-018-0544-x

Subcycle observation of lightwave-driven Dirac currents in a topological surface band

J. Reimann[1], S. Schlauderer[2], C. P. Schmid[2], F. Langer[2], S. Baierl[2], K. A. Kokh[3,4], O. E. Tereshchenko[4,5], A. Kimura[6], C. Lange[2], J. Güdde[1], U. Höfer[1]* & R. Huber[2]*

Harnessing the carrier wave of light as an alternating-current bias may enable electronics at optical clock rates[1]. Lightwave-driven currents have been assumed to be essential for high-harmonic generation in solids[2–6], charge transport in nanostructures[7,8], attosecond-streaking experiments[9–16] and atomic-resolution ultrafast microscopy[17,18]. However, in conventional semiconductors and dielectrics, the finite effective mass and ultrafast scattering of electrons limit their ballistic excursion and velocity. The Dirac-like, quasi-relativistic band structure of topological insulators[19–29] may allow these constraints to be lifted and may thus open a new era of lightwave electronics. To understand the associated, complex motion of electrons, comprehensive experimental access to carrier-wave-driven currents is crucial. Here we report angle-resolved photoemission spectroscopy with subcycle time resolution that enables us to observe directly how the carrier wave of a terahertz light pulse accelerates Dirac fermions in the band structure of the topological surface state of Bi_2Te_3. While terahertz streaking of photoemitted electrons traces the electromagnetic field at the surface, the acceleration of Dirac states leads to a strong redistribution of electrons in momentum space. The inertia-free surface currents are protected by spin–momentum locking and reach peak densities as large as two amps per centimetre, with ballistic mean free paths of several hundreds of nanometres, opening up a realistic parameter space for all-coherent lightwave-driven electronic devices. Furthermore, our subcycle-resolution analysis of the band structure may greatly improve our understanding of electron dynamics and strong-field interaction in solids.

The band structure of a crystalline solid describes the nontrivial energy–momentum relation of electrons that results from the overlap of orbitals of adjacent atoms. Because the band structure governs key physical and chemical properties of the solid, a complete understanding of it is important both for fundamental materials science and for applications. For instance, energy gaps distinguish insulators from metals, whereas the band slope sets the electron velocity. Angle-resolved photoemission spectroscopy (ARPES) can be used to map out the occupied part of band structures by measuring the kinetic energy of photoemitted electrons as a function of their momenta. One of the successes of ARPES is the experimental observation of three-dimensional topological

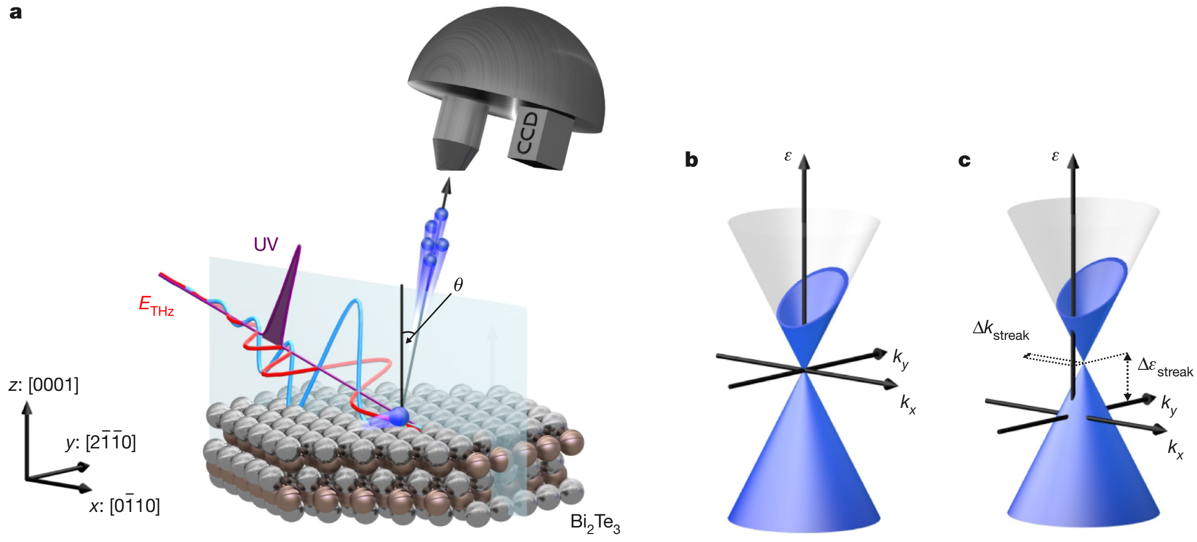

Fig. 1 | Concept of subcycle time-resolved ARPES. a, Electrons (blue spheres) in the topological surface state of Bi_2Te_3 (crystal lattice; brown spheres, Bi atoms; grey spheres, Te atoms) are accelerated by an intense linearly polarized THz field E_{THz} (red waveform, s-polarization; blue waveform, p-polarization) and are photoemitted by an ultrashort time-delayed p-polarized UV pulse (violet). The kinetic energy ε_{kin} and emission angle θ of the liberated electrons are measured by a hemispherical electron analyser to determine the binding energy and the parallel momentum k_y of the electrons in the topological surface band along the $\overline{\Gamma}-\overline{K}$ direction. The plane of incidence (x–z plane) is indicated by a transparent rectangle. **b**, Acceleration of Dirac fermions in the topological surface state can shift the Fermi surface. **c**, The interaction of the photoemitted electrons with the THz field in vacuum can manifest as a streaking of the photoemission spectra with an energy shift $\Delta\varepsilon_{streak}$ and/or a momentum shift Δk_{streak} of the apparent band structure.

---

[1]Department of Physics, Philipps-University of Marburg, Marburg, Germany. [2]Department of Physics, University of Regensburg, Regensburg, Germany. [3]V.S. Sobolev Institute of Geology and Mineralogy, Siberian Branch of the Russian Academy of Sciences, Novosibirsk, Russia. [4]Novosibirsk State University, Novosibirsk, Russia. [5]A.V. Rzhanov Institute of Semiconductor Physics, Siberian Branch of the Russian Academy of Sciences, Novosibirsk, Russia. [6]Graduate School of Science, Hiroshima University, Hiroshima, Japan. *e-mail: hoefer@physik.uni-marburg.de; rupert.huber@ur.de

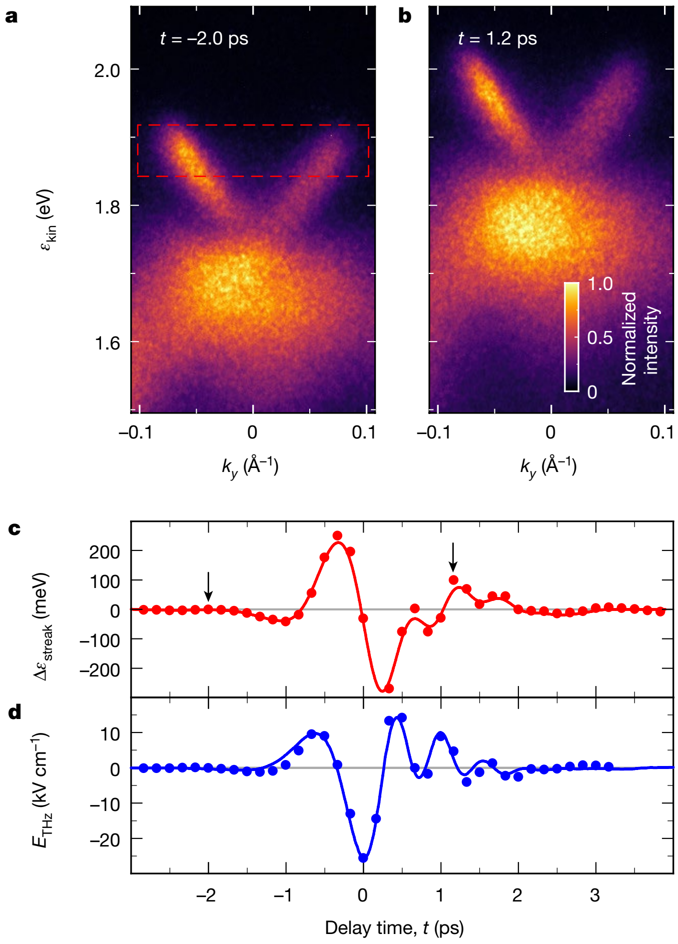

Fig. 2 | Energy streaking of the photoelectrons by p-polarized THz radiation. a, Photoemission map taken before the arrival of the THz field ($t = -2.0$ ps). The dashed red rectangle depicts the region that is traced to evaluate the time-dependent energy shift. **b**, Corresponding photoemission map taken 1.2 ps after the arrival of the maximum THz electric field, exhibiting THz streaking. **c**, Energy shift of the photoemission spectra as a function of the pump–probe delay time (red circles, experiment; solid curve, simulation; see text). The arrows indicate the delay times at which the photoemission maps in **a** and **b** are taken. **d**, Reconstructed electric field amplitude of the standing wave in front of the surface (blue circles). The blue solid curve shows the scaled and time-shifted electric field as measured externally by electro-optic sampling.

insulators[19–21] with unusual transport properties: owing to strong spin–orbit interaction, these solids are insulating in the bulk, but the surface exhibits gapless states that are protected by time-reversal symmetry[19]. The quasi-relativistic dispersion and a reduction in scattering, caused by spin–momentum locking, makes these surface states promising for use in ultrafast low-loss electronics. Yet, the motion of Dirac fermions driven by an electric field is not accessible by conventional photoemission spectroscopy.

By exploiting ultrashort laser pulses, time-resolved ARPES has been used to trace the dynamics of photo-injected currents at surfaces as a small imbalance of carriers moving in opposite directions[30]. ARPES has also revealed light-induced Floquet states[23] and interband transitions[22], specifically in topological insulators. Furthermore, attosecond metrology has been used to access subcycle time delays in the momentum-integrated photoemission from surfaces with known band structures[9–13,16]. A systematic understanding of electromagnetically driven intraband currents in materials with unknown electronic states and dynamics, such as topological insulators, requires an analysis of the band structure with subcycle resolution.

Here, we present a time-resolved ARPES study with subcycle resolution. We observe directly how an intense terahertz (THz) wave accelerates Dirac fermions in the quasi-relativistic band structure of the topological surface state of Bi$_2$Te$_3$. The inertia-free transient Dirac currents peak at a density of 2 A cm^{-1} with a maximum ballistic excursion of electrons in real space of several hundred nanometres. Our results open up a new chapter in lightwave electronics, whereby currents induced by optical carrier waves can be traced directly within the band structure.

The concept of our experiment is illustrated in Fig. 1a. A single crystal of Bi$_2$Te$_3$ is kept in an ultrahigh-vacuum (UHV) chamber. This material belongs to a class of three-dimensional topological insulators that exhibit a topological surface state with a single non-degenerate Dirac cone at the $\bar{\Gamma}$ point in the Brillouin zone[19,20]. A strong THz electric field (E_{THz}) is focused onto the surface to accelerate the Dirac fermions. This process is expected to shift the electron occupation in momentum space along the field direction (Fig. 1b). These dynamics should be strongly influenced by many-body interactions, such as scattering. In our experiment, we probe the transient electron distribution directly in momentum space via time- and angle-resolved photoemission. We use a time-delayed ultraviolet (UV) laser pulse (duration, 100 fs; centre wavelength, 201 nm) to release electrons out of the surface. An electrostatic hemispherical electron analyser, equipped with a charge-coupled device (CCD) detector, then images the relationship between the energy ε and the momentum k_y of the photoelectrons parallel to the surface (Fig. 1b). On their way to the detector, the electrons also interact with the THz field in the vacuum, so the apparent band structure is effectively offset in energy and momentum (Fig. 1c). Because the duration of the UV pulse is much shorter than the oscillation period of the THz driving field, this 'streaking' effect can be used to sample the electric field close to the surface, in a similar way to the sampling of near-infrared lightwaves by attosecond pulses[9–13,16]. The relative strength of intraband acceleration and streaking in vacuum can be controlled by the THz polarization.

In the first step, we show that THz fields polarized in the plane of incidence (p-polarization) predominantly lead to energy streaking of photoemitted electrons. In Fig. 2a, b we display angle-resolved photoemission spectra for two different delay times t between the p-polarized THz field and the UV probe. The characteristic V-shaped dispersion of Dirac fermions demonstrates the presence of a topological surface state, whereas the bulk valence band manifests as the broad dispersion at lower energies. The Fermi velocity that we deduce from the linear dispersion of the topological surface state, $\varepsilon(k_y) = \hbar v_{\mathrm{F}} k_y$, is $v_{\mathrm{F}} = 4.1$ Å fs^{-1} $= 410$ nm ps^{-1}. The THz field appears to offset the entire band structure in energy, while leaving its shape and momentum position largely unchanged. This behaviour is well explained considering that, for our Bi$_2$Te$_3$ sample, the Fresnel reflection at the surface (see Methods) leads to strong suppression of the THz field component in the sample plane and strong enhancement of the perpendicular component. The resulting, dominantly out-of-plane field causes pronounced energy streaking of photoemitted electrons, but cannot effectively accelerate Dirac fermions within the surface bands.

For a quantitative analysis, we extract the THz field from the experimental energy streaking $\Delta\varepsilon_{\mathrm{streak}}(t)$ (Fig. 2c, red circles), which we determine by tracing the energy position of a fixed cut-out of the photoemission intensity distribution (Fig. 2a, red dashed rectangle) as a function of time. For a given THz transient, $\Delta\varepsilon_{\mathrm{streak}}(t)$ can be calculated by integrating the classical equation of motion of an electron accelerated by the Lorentz force (see Methods). By inverting this relation, we retrieve the THz waveform $E_{\mathrm{THz}}(t)$ above the sample surface (Fig. 2d, blue circles). An integration of the equation of motion in the full three-dimensional THz field including the strongly screened in-plane component (Fig. 2c, red line) is in excellent agreement with the experimental shift $\Delta\varepsilon_{\mathrm{streak}}(t)$, confirming that the dynamics is dominated by the out-of-plane electric field. We also verify that the reconstructed THz transient coincides with the waveform determined

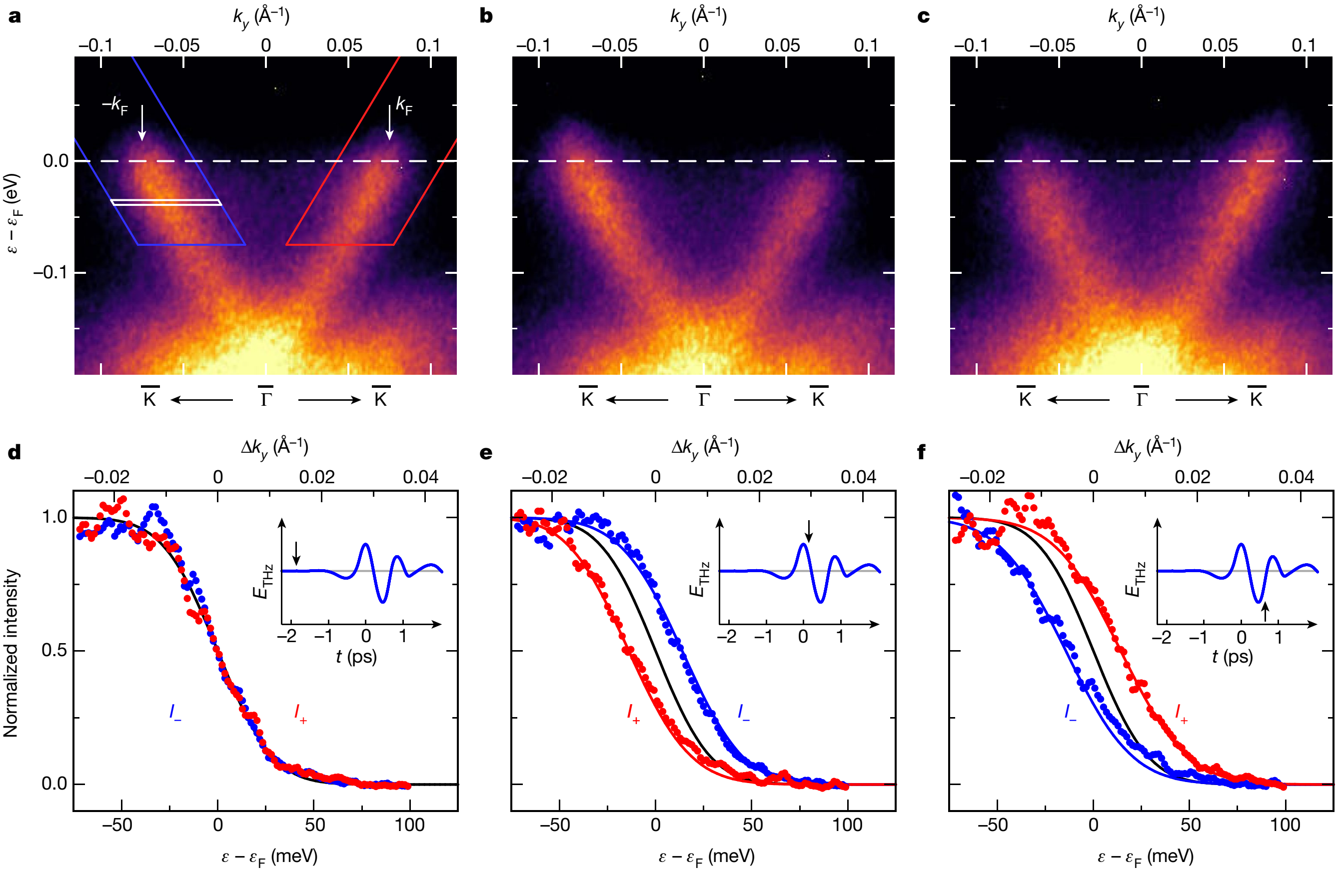

Fig. 3 | Acceleration of the electrons within the surface band by s-polarized THz radiation. a–c, Photoemission maps before the arrival of the THz field ($t = -1.86$ ps) (**a**), just after the first positive maximum of the electric field ($t = 0.14$ ps) (**b**) and immediately after the negative crest of the electric field ($t = 0.64$ ps) (**c**). The white dashed lines indicate the Fermi level for the unperturbed system; the Fermi wave vector k_F is indicated in **a**. **d–f**, Intensity distributions I_- and I_+ of the photoemission maps shown in **a–c** along the left (blue circles) and right (red circles) branches of the Dirac cone, respectively. I_- and I_+ are obtained by integrating the measured intensity over horizontal slices (see, for example, white box in **a**) moved along trapezoidal regions as depicted in **a**. The solid curves show the results of simulations based on the Boltzmann equation. The black curves depict the equilibrium situation and correspond to a Fermi–Dirac distribution at 80 K convoluted with the experimental energy resolution. The insets in **d–f** show the reconstructed electric field, with the black arrows indicating the delay times of the corresponding snapshots.

by electro-optic sampling outside the UHV chamber (Fig. 2d, blue line), which demonstrates the reliability of the field retrieval by streaking.

The electric field of s-polarized THz pulses is oriented along the y direction, in which our electron analyser detects the electron momentum k_y. Although streaking is strongly suppressed in this geometry because of screening of the THz field parallel to the surface, the remaining momentum streaking Δk_{streak} still allows us to probe the instantaneous field directly (see Methods). Moreover, the s-polarized, in-plane component may accelerate electrons within the topologically protected surface band. In Fig. 3a–c we display snapshots of photoemission spectra for three characteristic delay times t: before the THz transient (Fig. 3a), 0.14 ps after the positive field maximum (Fig. 3b) and 0.18 ps after the negative crest (Fig. 3c). For vanishing fields (Fig. 3a), the left and right branches of the Dirac cone are occupied up to the same Fermi energy ($\varepsilon_F \approx 200$ meV above the Dirac point) and Fermi momentum ($k_F = 0.075$ Å^{-1}). When the electric field is applied, the occupation becomes asymmetric.

More quantitatively, we extract the intensity distributions of photoelectrons along the left (I_-; blue circles) and right (I_+; red circles) branches of the Dirac cone (Fig. 3d–f). For each energy, $I_\pm$ is obtained by integrating the photoemission intensity over a narrow momentum interval (such as depicted by the white box in Fig. 3a) centred about the Dirac band. The normalized distributions $I_\pm(t)$ directly represent femtosecond snapshots of the population in each branch of the topological surface state, that is, the energy and momentum distributions $f(\varepsilon, t)$ and $f(k_y, t)$, respectively. Whereas the red and blue curves coincide with each other in the absence of an electric field (Fig. 3d), they are shifted horizontally in energy and momentum with respect to each other when the electric field is present (Fig. 3e, f). This shift is reversed when the electric field changes sign. The opposite shift of the population of the surface band for opposite electron momenta signifies an ultrafast displacement of the Fermi circle in momentum space. To the best of our knowledge, this marks the first direct observation of electron currents driven by the carrier wave of an ultrashort electromagnetic pulse in the band structure of a solid, in general, and of Dirac currents, in particular. As shown in Supplementary Video 1, we can even retrieve a complete quasi-continuous subcycle video of THz-driven Dirac fermions within their band structure. The transient shift of the electrons in momentum space results in a net current flowing in the positive or negative y direction on the surface of the sample.

The measured momentum distribution $f(k_y, t)$ allows us to identify the key mechanisms that govern the subcycle transport of the Dirac fermions directly in the time domain. Before the interaction with the THz field (Fig. 3d), the measured $I_\pm(k_y)$ is well described by a Fermi–Dirac distribution for our sample temperature of 80 K (solid line). Shortly after the field maxima (Fig. 3e, f), the curves are broadened and strongly displaced from their equilibrium distribution. Here, the transient electric field $E_{\text{THz}}(t)$ coherently accelerates the electrons out of equilibrium, while scattering limits their ballistic motion. This scenario can be described approximately by the semi-classical Boltzmann equation (see Methods), as shown by the blue and red solid lines in Fig. 3e, f.

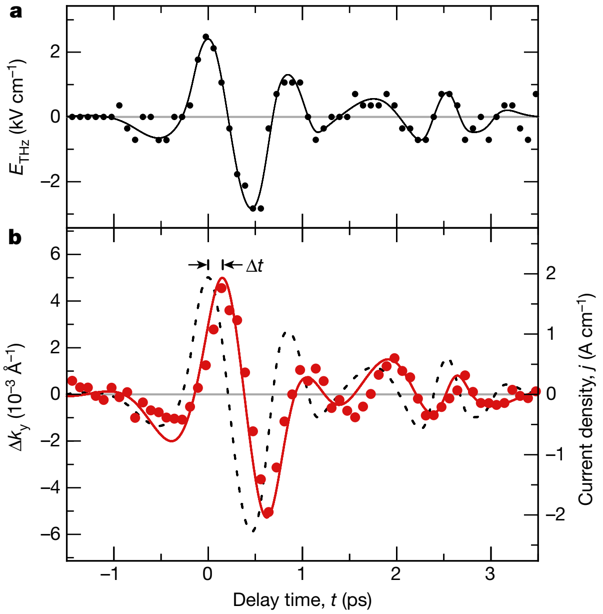

Fig. 4 | Dynamics of electric current within the surface band. **a**, Electric field parallel to the surface as reconstructed from the transient momentum shift of the photoelectrons (black circles). The black solid line is a spline through the data. **b**, Temporal evolution of the current density extracted from the photoemission intensity distributions (red circles). The red solid curve shows the simulated current dynamics calculated for scattering times of $\tau_{\mathrm{R}} = \tau_{k\bar{k}} = 1$ ps and the electric field transient of **a**, which is depicted in **b** by the dashed curve, for comparison.

Our model accounts for electron scattering in a simple relaxation-time approximation including Pauli exclusion. The scattering time for processes that relax the excess energy of an electron is τ_{R}; the time for elastic scattering between $+k_y$ and $-k_y$ is quantified by $\tau_{k\bar{k}}$. In the presence of a driving field, both effects tend to push the carriers towards a Fermi–Dirac distribution that is shifted in energy and momentum by the driving field (see Methods); the influence of scattering is remarkably weak in our experiment. This becomes obvious when we fit our model calculation to reproduce the experiment by adapting τ_{R} and $\tau_{k\bar{k}}$ and by scaling the electric field strength within the estimated experimental uncertainty. We achieve quantitative agreement (see, for example, Fig. 3e) only if both τ_{R} and $\tau_{k\bar{k}}$ are kept above 1 ps. Assuming scattering times as long as 2 ps (ref. [22]) deteriorates the agreement with the experiment only slightly, whereas shorter scattering times result in substantially different carrier distributions and/or weaker deflection than observed experimentally (see Methods).

The low scattering rate allows for a large displacement of the Fermi circle even for moderate peak fields of 2.4 kV cm^{-1} (Fig. 3b). In combination with the quasi-relativistic band structure, this situation results in extremely large current densities. With a maximum observed momentum shift of 0.005 Å^{-1}, we retrieve a peak surface current density of up to 2 A cm^{-1} (see Methods). This current flows within an atomically thin surface sheet that hosts the wavefunction of the topological surface state. Assuming a thickness of 1 nm, the corresponding bulk current density reaches values of up to 2×10^7 A cm^{-2}, or 4 nA per atom of the surface layer.

By repeating this analysis for various delay times t, we map out the subcycle dynamics of the current density $j(t)$ (Fig. 4b, red circles) together with the instantaneous THz field (Fig. 4b, dashed curve; Fig. 4a, black circles). The current density clearly shows the fingerprints of ballistic acceleration: $j(t)$ increases monotonically during the onset of the first intense THz half cycle. Although $E_{\mathrm{THz}}(t)$ decreases for $t > 0$ ps, $j(t)$ keeps rising and reaches its maximum at $t = 0.15$ ps, shortly before the reversal of the driving field. This behaviour, which also occurs for all other THz half cycles, is expected only when the influence of scattering on the Dirac current is weak. Solving the Boltzmann equation for the experimentally measured THz driving field reproduces the current dynamics very well, including the delayed response and the details of the subsequent current oscillations (Fig. 4b, solid curve). Again, we find the optimum agreement for scattering times τ_{R} and $\tau_{k\bar{k}}$ above 1 ps. The actual scattering times may well be even longer, but the limited time window of a THz half cycle makes determining an upper bound challenging. These values readily exceed coherence times observed previously for lightwave-driven electron dynamics in semiconductors and dielectrics[2–6] by two orders of magnitude and attest to a reduced scattering phase space due to spin–momentum locking. It would be particularly interesting to contrast these results with future subcycle ARPES of Dirac fermions in graphene, which lacks spin–momentum locking.

These unique transport dynamics of topological Dirac fermions elevate carrier-wave electronics to the all-coherent level. In contrast to the massive quasiparticles that populate the parabolic bands of conventional dielectrics, the acceleration of quasi-relativistic topological surface states is inertia-free because the group velocity of Dirac fermions is very high from the outset. Hence, THz-accelerated Dirac fermions may propagate coherently over several hundred nanometres before undergoing scattering (see Extended Data Fig. 5). This scale exceeds electron excursions in dielectrics[2–6] and the gate width of state-of-the-art electronic transistors by orders of magnitude. Therefore, we anticipate that devices based on three-dimensional topological insulators will soon exploit all-coherent electron transfer at THz or even petahertz clock rates, and that the underlying subcycle currents may become accessible to complementary real-space measurements[27].

In conclusion, we resolve the momentum distribution of Dirac fermions directly as they are accelerated by the carrier wave of a THz pulse within the band structure of the topological surface state. The combination of quasi-relativistic dispersion and spin–momentum locking makes topological insulators ideal for ultrafast electronics: inertia-free charge currents and unprecedented coherence lengths move microelectronic devices driven by lightwaves in a broad spectral range into practical reach. The extremely low dissipation rate of the currents that we observed practically eliminates limitations imposed by Joule heating (see Methods), so the speed of future devices is limited only by the optical clock rate of the light pulse, which could be scaled to ever higher frequencies, facilitating ultimately fast electronics. The linear dispersion relation of Dirac fermions may even enable dispersion-free wave-packet motion. Owing to spin–momentum locking, the ballistic Dirac currents should carry a spin current, which should enable spintronics up to optical clock rates. Finally, our concept of subcycle ARPES provides a way of observing carrier transport directly in non-trivial band structures. This idea may herald a new era of time-domain investigations of surface and bulk band structures of new materials and phenomena, ranging from topology to high-temperature superconductivity.

Online content

Any methods, additional references, Nature Research reporting summaries, source data, statements of data availability and associated accession codes are available at https://doi.org/10.1038/s41586-018-0544-x.

Received: 20 March 2018; Accepted: 26 July 2018;

1. Krausz, F. & Stockman, M. I. Attosecond metrology: from electron capture to future signal processing. *Nat. Photon*. **8**, 205–213 (2014).
2. Vampa, G. et al. Linking high-harmonics from gases and solids. *Nature* **522**, 462–464 (2015).
3. Hohenleutner, M. et al. Real-time observation of interfering crystal electrons in high-harmonic generation. *Nature* **523**, 572–575 (2015).
4. Langer, F. et al. Lightwave-driven quasiparticle collisions on a subcycle timescale. *Nature* **533**, 225–229 (2016).
5. Garg, M. et al. Multi-petahertz electronic metrology. *Nature* **538**, 359–363 (2016).
6. Liu, H. et al. High-harmonic generation from an atomically thin semiconductor. *Nat. Phys*. **13**, 262–265 (2017).
7. Rybka, T. et al. Sub-cycle optical phase control of nanotunnelling in the single-electron regime. *Nat. Photon*. **10**, 667–670 (2016).

8. Higuchi, T., Heide, C., Ullmann, K., Weber, H. B. & Hommelhoff, P. Light-field-driven currents in graphene. *Nature* **550**, 224–228 (2017).
9. Miaja-Avila, L. et al. Laser-assisted photoelectric effect from surfaces. *Phys. Rev. Lett.* **97**, 113604 (2006).
10. Cavalieri, A. L. et al. Attosecond spectroscopy in condensed matter. *Nature* **449**, 1029–1032 (2007).
11. Schultze, M. et al. Attosecond band-gap dynamics in silicon. *Science* **346**, 1348–1352 (2014).
12. Neppl, S. et al. Direct observation of electron propagation and dielectric screening on the atomic length scale. *Nature* **517**, 342–346 (2015).
13. Locher, R. et al. Energy-dependent photoemission delays from noble metal surfaces by attosecond interferometry. *Optica* **2**, 405–410 (2015).
14. Siek, F. et al. Angular momentum-induced delays in solid-state photoemission enhanced by intra-atomic interactions. *Science* **357**, 1274–1277 (2017).
15. Feist, A. et al. Quantum coherent optical phase modulation in an ultrafast transmission electron microscope. *Nature* **521**, 200–203 (2015).
16. Tao, Z. et al. Direct time-domain observation of attosecond final-state lifetimes in photoemission from solids. *Science* **353**, 62–67 (2016).
17. Cocker, T. L. et al. An ultrafast terahertz scanning tunnelling microscope. *Nat. Photon.* **7**, 620–625 (2013).
18. Cocker, T. L., Peller, D., Yu, P., Repp, J. & Huber, R. Tracking the ultrafast motion of a single molecule by femtosecond orbital imaging. *Nature* **539**, 263–267 (2016).
19. Hasan, M. Z. & Kane, C. L. Colloquium: Topological insulators. *Rev. Mod. Phys.* **82**, 3045–3067 (2010).
20. Zhang, H. J. et al. Topological insulators in Bi_2Se_3, Bi_2Te_3 and Sb_2Te_3 with a single Dirac cone on the surface. *Nat. Phys.* **5**, 438–442 (2009).
21. Chen, Y. L. et al. Experimental realization of a three-dimensional topological insulator, Bi_2Te_3. *Science* **325**, 178–181 (2009).
22. Kuroda, K., Reimann, J., Güdde, J. & Höfer, U. Generation of transient photocurrents in the topological surface state of Sb_2Te_3 by direct optical excitation with midinfrared pulses. *Phys. Rev. Lett.* **116**, 076801 (2016).
23. Mahmood, F. et al. Selective scattering between Floquet–Bloch and Volkov states in a topological insulator. *Nat. Phys.* **12**, 306–310 (2016).
24. Olbrich, P. et al. Room-temperature high-frequency transport of Dirac fermions in epitaxially grown Sb_2Te_3- and Bi_2Te_3-based topological insulators. *Phys. Rev. Lett.* **113**, 096601 (2014).
25. Souma, S. et al. Direct measurement of the out-of-plane spin texture in the Dirac-cone surface state of a topological insulator. *Phys. Rev. Lett.* **106**, 216803 (2011).
26. Sobota, J. A. et al. Ultrafast optical excitation of a persistent surface-state population in the topological insulator Bi_2Se_3. *Phys. Rev. Lett.* **108**, 117403 (2012).
27. Kastl, C., Karnetzky, C., Karl, H. & Holleitner, A. W. Ultrafast helicity control of surface currents in topological insulators with near-unity fidelity. *Nat. Commun.* **6**, 6617 (2015).
28. Minami, Y. et al. Terahertz-induced acceleration of massive Dirac electrons in semimetal bismuth. *Sci. Rep.* **5**, 15870 (2015).
29. Braun, L. et al. Ultrafast photocurrents at the surface of the three-dimensional topological insulator Bi_2Se_3. *Nat. Commun.* **7**, 13259 (2016).
30. Güdde, J., Rohleder, M., Meier, T., Koch, S. W. & Höfer, U. Time-resolved investigation of coherently controlled electric currents at a metal surface. *Science* **318**, 1287–1291 (2007).

Acknowledgements We thank R. Höfer for discussions. The work in Marburg was supported by the Deutsche Forschungsgemeinschaft (DFG) through SFB 1083 and grant number HO 2295/7 (SPP 1666). Work in Regensburg was supported by the DFG through grant numbers HU 1598/2-1 and SFB 1277 (Project A05) and by the European Research Council through grant number 305003 (QUANTUMsubCYCLE). O.E.T. and K.A.K. were supported by the Russian Science Foundation (project number17-12-01047). A.K. was financially supported by KAKENHI number 17H06138.

Reviewer information *Nature* thanks I. Katayama, S. Zhou and the other anonymous reviewer(s) for their contribution to the peer review of this work.

Author contributions J.G., U.H. and R.H. conceived the study. J.R., S.S., C.P.S., F.L., S.B. and J.G. carried out the experiment. K.A.K., O.E.T. and A.K. provided the samples and performed the transport measurements. J.R., C.L., J.G. and U.H. carried out the theoretical modelling. All authors analysed the data, discussed the results and contributed to writing the manuscript.

Competing interests The authors declare no competing interests.

Additional information

Extended data is available for this paper at https://doi.org/10.1038/s41586-018-0544-x.

Supplementary information is available for this paper at https://doi.org/10.1038/s41586-018-0544-x.

Reprints and permissions information is available at http://www.nature.com/reprints.

Correspondence and requests for materials should be addressed to U.H. or R.H.

METHODS

Experimental set-up. We start with near-infrared pulses (centre wavelength, 807 nm; pulse energy, 5.5 mJ; pulse duration, 33 fs) from a titanium:sapphire amplifier (repetition rate, 3 kHz). Part of the laser output is used to generate intense THz pulses (pulse energy, 1 μJ) by tilted-pulse front optical rectification[31] in a cryogenically cooled lithium niobate ($LiNbO_3$) crystal (Extended Data Fig. 1a). A pair of wire-grid polarizers controls the polarization direction of the THz field. A typical transient after transmission through the fused silica window of the vacuum chamber is shown in Extended Data Fig. 1b. A second branch of the laser output is frequency-converted into the UV to release photoelectrons from the sample surface. To this end, we generate the fourth harmonic by cascaded sum-frequency generation with the fundamental amplifier pulses in β-barium borate (β-BBO) crystals (Extended Data Fig. 1c). Extended Data Fig. 1d depicts a typical resulting spectrum. A prism sequence separates the fourth harmonic from the fundamental pulses and pre-compensates for the material dispersion of the window of the vacuum chamber. The THz and UV pulses are spatially overlapped with a custom-built gold mirror featuring an aperture for the transmission of the UV pulses. A mechanical delay stage in the excitation beam path allows us to temporally delay THz and UV pulses with respect to each other. The fluence of the UV light is set by detuning the wave plate in front of the third-harmonic generation crystal (see Extended Data Fig. 1c). The collinear THz-pump and p-polarized UV-probe pulses are transmitted through a UV-grade fused silica window into a μ-metal shielded UHV chamber at a base pressure of 7×10^{-11} mbar. A spherical UV-grade aluminium mirror (focal length, 75 mm) mounted within the UHV chamber is used to focus both beams under an angle of incidence of 53° onto the sample. Photoelectrons are collected along the high-symmetry line $\overline{\Gamma}-\overline{K}$ perpendicular to the plane of light incidence by a hemispherical electron analyser with a display-type detector (Specs Phoibos 150). The energy resolution of the set-up is 45 meV (full-width at half-maximum), mainly limited by the bandwidth of the UV pulses. Energy and momentum shifts of photoelectrons can be determined with an accuracy of 3 meV and 0.004 $Å^{-1}$, respectively.

Sample preparation and characterization. The Bi_2Te_3 samples are fabricated by using the modified Bridgman method[32]. By choosing an appropriate solidification condition, a gradation in the carrier concentration was realized in an ingot naturally forming a p–n junction. Transport measurements within the temperature range of 10–300 K reveal a carrier mobility of about 10^4 cm^2 V^{-1} s^{-1} at 4 K, indicating the high crystal quality. The longitudinal resistance at 80 K is about 0.4 mΩ cm^{-1}. It increases with temperature, confirming bulk conductive characteristics. A clean and well-ordered surface is obtained by cleaving the sample in situ using the Scotch tape method at a pressure of 3×10^{-10} mbar followed by a rapid recovery back to the base pressure within 1 min. During the measurements the sample temperature is maintained at 80 K. The Dirac point of the sample is located 200 meV below the Fermi energy.

Reconstruction of p-polarized THz radiation. The electric field component of the p-polarized THz transient is reconstructed from the measured photoelectron energy streaking by considering the classical motion of the photoelectrons in the electric and magnetic fields of the THz transient in vacuum. The transient Lorentz force on a photoemitted electron due to the electric and magnetic field components of the THz transient is

$$\boldsymbol{F}(t) = -e\boldsymbol{E}(t) - e\boldsymbol{v}(t) \times \boldsymbol{B}(t)$$

Here, e is the elementary charge, $\boldsymbol{v}(t)$ the velocity of the electron, and $\boldsymbol{E}(t)$ and $\boldsymbol{B}(t)$ are the electric and magnetic field components of the THz transient. Because the amplitude of the magnetic field component in vacuum is $B_0 = E_0/c$ and $v \ll c$, we can neglect the magnetic contribution to the Lorentz force; the velocity of the electron is then

$$\boldsymbol{v}(t) = -\frac{e}{m}\int_t^{\infty} \boldsymbol{E}(t')\mathrm{d}t' + \boldsymbol{v}_0$$

where m is the electron mass, $\boldsymbol{v}_0$ is the initial velocity of the photoemitted electrons and t is the time of photoemission. We note that $\boldsymbol{v} = \boldsymbol{v}_0$ not only when the photoemission UV pulse arrives after the THz transient has already left the surface, but also when the UV pulse precedes the complete THz transient as the time-averaged acceleration of the complete electric field transient on the electron in the vacuum vanishes.

With kinetic energy $\varepsilon_{\mathrm{kin}}(t) = (1/2)m[\boldsymbol{v}(t)]^2$, the temporal change in the kinetic energy caused by the electric field is

$$\frac{\mathrm{d}\varepsilon_{\mathrm{kin}}(t)}{\mathrm{d}t} = -e\boldsymbol{v}(t) \cdot \boldsymbol{E}(t)$$

In the case of normal emission and screening of the electric field component parallel to the surface, this can be rewritten as

$$\frac{\mathrm{d}\varepsilon_{\mathrm{kin}}(t)}{\mathrm{d}t} = -e\sqrt{2m\varepsilon_{\mathrm{kin}}(t)}\,E_{\perp}(t)$$

where $E_{\perp}(t)$ is the magnitude of the standing wave perpendicular to the surface. Thus, we can quantitatively determine the strength of the electric field along the surface normal directly from the observed transient change in the kinetic energy of the electron using

$$E_{\perp}(t) = -\frac{\mathrm{d}\varepsilon_{\mathrm{kin}}(t)}{\mathrm{d}t}\left[2me^2\varepsilon_{\mathrm{kin}}(t)\right]^{-1/2}$$

Reconstruction of s-polarized THz radiation. The s-polarized electric field is oriented parallel to the surface, along the direction in which our electron analyser detects the component of the electron momentum parallel to the surface ($\hbar k_y$). Streaking is strongly supressed in this geometry because of the screening of the THz field parallel to the surface. Nevertheless, the photoemitted electrons acquire a small additional parallel momentum

$$\Delta p(t) = -e\int_t^{\infty} E(t')\mathrm{d}t'$$

leading to an overall momentum shift of the photoelectron spectrum. In addition, they experience a small energy shift $\Delta\varepsilon = \Delta p v_{0,\parallel}$ proportional to their initial parallel velocity $v_{0,\parallel}$. As a result, the photoelectron spectra of the Dirac cone appear not only shifted in k_y direction but also slightly tilted. This tilt can in principle be used to distinguish the acceleration of electrons by the electric field in the solid (which affects only electrons in the vicinity of the Fermi level) from the acceleration after photoemission (which affects all electrons). In our experiment, the parallel velocity of electrons photoemitted from the Fermi level ($\hbar k_{\mathrm{F}}/m = 0.87$ Å fs^{-1}) is much smaller than their velocity in the solid ($v_{\mathrm{F}} = 4.1$ Å fs^{-1}). The observed transient energy gains and losses of electrons near k_{F} due to the s-polarized THz field are thus dominated by the acceleration inside the solid and we refrain from applying the corresponding correction to the data.

The small momentum streaking, however, allows us to track the instantaneous THz field in the case of s-polarized THz radiation using

$$E_{\parallel}(t) = -\frac{\hbar}{e}\frac{\mathrm{d}k_{\mathrm{streak}}}{\mathrm{d}t}$$

where $\mathrm{d}k_{\mathrm{streak}}/\mathrm{d}t$ is the transient momentum shift of the whole photoemission spectrum. At the maximum field amplitude, the observed transient momentum shift was 0.043 ± 0.009 $Å^{-1}$ ps^{-1}, corresponding to a THz field of $E_{\parallel,\mathrm{max}} = 2.8 \pm 0.5$ kV cm^{-1}. Because the parallel component of the electric field in the surface region of the sample is the same as in the vacuum, momentum streaking provides an accurate and direct way of determining the actual strength of the acceleration field that acts on the electrons in the topological surface state.

This field strength can be verified independently by using the Fresnel coefficients[33] of the Bi_2Te_3 sample and the field extracted for p-polarized pulses. To this end, we first compare p-polarized THz waveforms reflected from Bi_2Te_3 and a gold reference by using electro-optic sampling (see Extended Data Fig. 2a). The ratio of the amplitude spectra of the two transients (Extended Data Fig. 2b) yields the reflection coefficient r_{p} (see Extended Data Fig. 2c, black spheres). r_{p} is rather high over the measured frequency range—similar to metals—and has three minima, which we attribute to phonon resonances[34]. Consequently, we model the underlying dielectric function $\epsilon(\omega)$ with the response of a free-electron plasma and three Lorentzian oscillators:

$$\epsilon(\omega) = \epsilon_{\infty} - \frac{\omega_{\mathrm{p}}^2}{\omega^2 + i\omega/\tau} + \frac{A_1}{\omega_1^2 - \omega^2 - i\omega\gamma_1} + \frac{A_2}{\omega_2^2 - \omega^2 - i\omega\gamma_2} + \frac{A_3}{\omega_3^2 - \omega^2 - i\omega\gamma_3} \quad (1)$$

where ϵ_{∞} is the high-frequency limit of the dielectric function, ω_{p} denotes the plasma frequency and τ is the damping of the Drude term. Moreover, the three Lorentz oscillators are characterized by the resonance frequencies ω_1, ω_2 and ω_3, the oscillator strengths A_1, A_2 and A_3, and the damping rates γ_1, γ_2 and γ_3. The values for the phonon frequencies and damping rates are taken from elsewhere[34], and the value for the plasma frequency is taken from the independent transport measurement discussed above. Varying A_1, A_2 and A_3 allows us to fit (Extended Data Fig. 2c, orange curve) the experimentally measured reflection coefficient. Because the p-polarized THz waveform of Fig. 2d recorded by energy streaking is the superposition of incident and reflected fields[33], r_p allows us to deduce the incident field transient. When we assume the same incident waveform in s-polarization (corrected by a scaling factor of 2 set by the wire-grid polarizers) and compute[33] the transmission coefficient t_s (Extended Data Fig. 2d) from the dielectric function of equation (1), we obtain the internal field in s-polarization. The peak amplitude parallel to the surface is found to be $E_{\parallel,\max} = 4.0 \pm 1.5$ kV cm^{-1}, which indeed lies within the error margins of the value obtained directly by photoelectron streaking (Fig. 4a).

Calculation of the current density. The current density of two-dimensional Dirac electrons is given by the k-space integral

$$\boldsymbol{j} = -\nu e v_{\mathrm{F}} \int \frac{\mathrm{d}^2 k}{(2\pi)^2} f(\boldsymbol{k})\hat{\boldsymbol{k}} \qquad (2)$$

where $f(\boldsymbol{k})$ is the momentum distribution function, $\hat{\boldsymbol{k}}$ is a unit vector and ν denotes the number of electrons per surface unit cell ($\nu = 1$ for a topological surface state). In this expression we have exploited the fact that all electrons travel with the same group velocity, $\boldsymbol{v}(\boldsymbol{k}) = \boldsymbol{v}_{\mathrm{F}} = v_{\mathrm{F}}\hat{\boldsymbol{k}}$, owing to the linear dispersion of the Dirac cone. Moreover, neglecting the weak spin-Hall effect, $f(\boldsymbol{k})$ stays symmetric in the k_x direction with an applied field in the y direction. Therefore, accurate values for $\boldsymbol{j}(t)$ can be deduced directly from the experimental data by numerical integration using the measured snapshots of $f(k_y, t)$ and the measured value of the Fermi velocity, $v_{\mathrm{F}} = 4.1$ Å fs^{-1}.

An approximate value of the magnitude of $\boldsymbol{j}$ is obtained by considering that the observed shifts of $f(k_y, t)$ in the y direction (Δk), although large on an absolute scale, are small relative to the Fermi momentum k_{F}. Because the widening of f due to scattering is also small compared to k_{F}, evaluation of equation (2) yields $j \approx -e v_{\mathrm{F}} k_{\mathrm{F}} \Delta k/(4\pi)$. With the two-dimensional electron density $n = -k_{\mathrm{F}}^2/(4\pi)$, the approximate current density becomes $j \approx -e v_{\mathrm{F}} n \Delta k / k_{\mathrm{F}}$. With the experimental value of $k_{\mathrm{F}} = 0.075$ Å^{-1}, the electron density in the upper part of the Dirac cone of the topological surface state of our sample amounts to $n = 4.5 \times 10^{-4}$ Å$^{-2} = 4.5 \times 10^{12}$ cm^{-2}. For the maximum observed momentum shift of $\Delta k = 0.005$ Å^{-1}, a substantial fraction of $2\Delta k/k_{\mathrm{F}} = 13\%$ of these electrons carry the current. The current density thus reaches values as high as $j = 0.12e$ ps^{-1} Å$^{-1} = 2.0$ A cm^{-1}. We anticipate that these femtosecond currents may also become accessible to complementary real-space measurements[27] once subcycle resolution has been reached by these techniques.

Modelling electron scattering using the Boltzmann equation. The Boltzmann equation for electrons in a two-dimensional surface state accelerated by a time-dependent electric field $\boldsymbol{E}(t)$ parallel to the surface has the form

$$\frac{\partial f(\boldsymbol{k},t)}{\partial t} = -\frac{e}{\hbar}\boldsymbol{E}(t)\cdot\boldsymbol{\nabla}_{\boldsymbol{k}} f(\boldsymbol{k},t) + \left[\frac{\partial f(\boldsymbol{k},t)}{\partial t}\right]_{\text{scattering}} \qquad (3)$$

The first term on the right describes the redistribution of electrons in k space in the presence of $\boldsymbol{E}(t)$. The second term includes all changes in $f(\boldsymbol{k}, t)$ due to electron scattering within the surface state. Scattering into and out of bulk electronic states as well as electron diffusion from the topological surface state into the bulk are absent under the conditions of our experiment because the acceleration field does not lift the electrons above the bulk bandgap of $\mathrm{Bi_2Te_3}$ (energy gain less than 25 meV).

For the simulation, we compose the scattering term from two phenomenological contributions:

$$\left[\frac{\partial f(\boldsymbol{k},t)}{\partial t}\right]_{\text{scattering}} = -\frac{f(\boldsymbol{k},t) - f_0(\boldsymbol{k})}{\tau_{\mathrm{R}}} - \frac{f(\boldsymbol{k},t) - f(-\boldsymbol{k},t)}{\tau_{k\bar{k}}} \qquad (4)$$

Microscopically, the first term describes elastic and inelastic electron scattering within the relaxation-time approximation and equilibrates the accelerated electrons, where

$$f_0(\boldsymbol{k}) = \frac{1}{\exp[\beta(\hbar v_{\mathrm{F}}\,|\boldsymbol{k}| - \mu)] + 1}$$

is the equilibrium momentum distribution before the arrival of the THz pulse, μ is the chemical potential (Fermi level), $\beta = 1/(k_{\mathrm{B}}T)$ is the inverse temperature and τ_{R} is a phenomenological relaxation time. In general, τ_{R} should depend on $\boldsymbol{k}$ because, for example, the phase space for inelastic scattering is a function of the momentum along the Dirac cone. However, the momentum interval around k_{F} in which $f(\boldsymbol{k}, t)$ changes is still sufficiently small for scattering to be approximated by a single parameter τ_{R}. The second, purely elastic scattering term drives the accelerated Dirac fermions into a hot quasi-equilibrium distribution. Here, multiple scattering processes are involved microscopically because direct backscattering from $\boldsymbol{k}$ to $-\boldsymbol{k}$ is strongly supressed in a topological surface state as it would require a spin flip[19]. The time constant $\tau_{k\bar{k}}$ represents an effective phenomenological backscattering time due to multiple individual scattering events.

We first discuss the effect of the relaxation term, neglecting the second term in equation (4). The time-dependent Boltzmann equation (equation (3)) can then be transformed into an ordinary differential equation and solved by direct integration. For small relaxation times τ_{R}, the solution is

$$f(\boldsymbol{k},t) \approx \frac{1}{\exp\{\beta[\hbar v_{\mathrm{F}}\,|\boldsymbol{k}| - \mu - e\boldsymbol{v}_{\mathrm{F}}\cdot\boldsymbol{E}(t)\tau_{\mathrm{R}}]\} + 1}$$

In this limit, $f(\boldsymbol{k}, t)$ is just the initial distribution $f_0(\boldsymbol{k}) = f(\boldsymbol{k}, 0)$ shifted in energy by an amount proportional to the Fermi velocity v_{F} of the Dirac electrons, the scattering time τ and the momentary strength of the electric field $\boldsymbol{E}(t)$. In k space, this energy shift corresponds to $\Delta k = eE\tau_{\mathrm{R}}/\hbar$. This is the same result as usually derived by considering the stationary case $\partial f(\boldsymbol{k}, t)/\partial t = 0$ for a slowly varying electric field and with the assumption that under the presence of the electric field $f(\boldsymbol{k})$ does not deviate much from the unperturbed distribution $f_0(\boldsymbol{k})$ (ref. [35]). Likewise, the shape of $f(\boldsymbol{k}, t)$ does not deviate from $f_0(\boldsymbol{k})$ for large scattering times τ_{R} and is merely shifted by an amount proportional to v_{F} and the time-integrated force acting on the electrons.

In our case, the temporal variation of the electric field $\boldsymbol{E}(t)$ occurs on a timescale similar to the relaxation time τ_{R}. Then the distribution $f(\boldsymbol{k}, t)$ not only is shifted in k space but also attains a shape that deviates from the initial Fermi–Dirac distribution $f_0(\boldsymbol{k})$. However, for not too large electric fields, these deviations remain small (Extended Data Fig. 3a-f). By contrast, we observe experimentally that $f(k_y, t)$ widens substantially for longer delays. The broadening is clearly visible in Fig. 3f, and in our experiment (Extended Data Fig. 4) is most obvious at delay times where Δk goes through zero (Extended Data Fig. 4b). To account for this additional broadening, we add the second scattering term in equation (4). The Boltzmann equation (equation (3)) with this backscattering term alone would be able to reproduce the experimentally observed time-dependent shift in $f(\boldsymbol{k}, t)$. In this model, however, the width of the distribution can only increase but not decrease as a function of time (Extended Data Fig. 3g–l). Experimentally, we observe that for delays exceeding 2.5 ps the width has relaxed to its initial value (Extended Data Fig. 4c). For these reasons both terms in equation (4) are necessary in the most basic model description.

Although the assumptions of our phenomenological model are strong simplifications for excitation far from equilibrium, the approach is able to describe the experimental data well (compare Fig. 3e, f and Fig. 4b). Moreover, the experimental determination of the amplitude and of the exact phase of the accelerating field $\boldsymbol{E}(t)$ by means of momentum streaking puts firm lower bounds on the scattering times. Assuming higher field strengths would require faster scattering for the model to reproduce the measured momentum shift of $f(ky, t)$ and the respective current density $j(t)$. However, the simulated curves then precede the measured ones in time. We achieve best overall agreement between experiment and simulation when a time constant for effective backscattering $\tau_{k\bar{k}}$ is chosen that is of similar magnitude (about 1 ps) to the relaxation time τ_{R}.

Joule heating. The Joule heating of the sample by the generated electron current is extremely small, as can be seen from the following. With a current density of $j = 2$ A cm^{-1}, as has been generated in an accelerating field of $E = 2.4$ kV cm^{-1}, the energy dissipated by one THz pulse within its duration of $\Delta t = 2.5$ ps amounts only to $W = jE\Delta t = 0.01$ μJ cm^{-2}. This value is several orders of magnitude lower than the absorbed fluence in a usual optical pump–probe experiment. Even if we neglect heat diffusion and assume that the dissipated heat stays within the topmost quintuple layer of $\mathrm{Bi_2Te_3}$ ($d = 1$ nm), the temperature rise associated with this energy is only $\Delta T = W/(dc_{\mathrm{p}}) = 0.1$ K, where we assume $c_{\mathrm{p}} = 1.001$ J cm^{-3} K^{-1} as the volumetric heat capacity of $\mathrm{Bi_2Te_3}$ at 80 K, calculated from the specific heat of 103.58 J mol^{-1} K^{-1} (ref. [36]), a molar mass of $M = 800.761$ g mol^{-1} and the density of $\rho = 7.74$ g cm^{-3}.

Calculation of the current excursion within the topologically protected surface band. From the two-dimensional current density j and the scattering times τ_{R} and $\tau_{k\bar{k}}$ of the Dirac fermions, we can retrieve the microscopic evolution of the current density within the surface layer of $\mathrm{Bi_2Te_3}$. In a first step, we calculate the total scattering time as

$$\tau_{\mathrm{t}} = \left(\frac{1}{\tau_{\mathrm{R}}} + \frac{2}{\tau_{k\bar{k}}}\right)^{-1}$$

Dirac fermions propagating at a velocity of $v_{\mathrm{F}} = 4.1$ Å fs^{-1} will then have a mean free path of $l = v_{\mathrm{F}}\tau_{\mathrm{t}} = 137$ nm. According to the scattering-time approximation (equation (4)), a current created at location $y = 0$, would then decay exponentially with a decay constant of 137 nm. To visualize this situation, we consider the accelerating action of the THz electric field only at $y = 0$ and let the current propagate freely elsewhere. With the current density $j(t) = j(y = 0, t)$ (Fig. 4b, red curve) extracted from the Boltzmann equation (see equation (3)), we can calculate the full spatial and temporal dynamics of the current density $j(y, t)$ as

$$j(y,t) = j_0\left(t - \frac{y}{v_{\mathrm{F}}}\right)\mathrm{e}^{-y/l}$$

Extended Data Fig. 5a displays $j(y, t)$ (colour scale) in the surface layer of Bi_2Te_3. A sizable fraction of the initial current density survives even after a propagation length as large as 0.5 μm.

Data availability

The data that support the findings of this study are available from the corresponding authors on request.

31. Hebling, J., Yeh, K.-L., Hoffmann, M. C., Bartal, B. & Nelson, K. A. Generation of high-power terahertz pulses by tilted-pulse-front excitation and their application possibilities. *J. Opt. Soc. Am. B* **25**, 6–19 (2008).
32. Kokh, K. A. et al. Melt growth of bulk Bi_2Te_3 crystals with a natural p-n junction. *CrystEngComm* **16**, 581–584 (2014).
33. Hecht, E. *Optics* 4th edn, Ch. 4 (Pearson Addison-Wesley, New York, 2012).
34. Richter, W., Köhler, H. & Becker, C.R. Raman and far-infrared investigation of phonons in the rhombohedral V_2-VI_3 compounds Bi_2Te_3, Bi_2Se_3, Sb_2Te_3 and $Bi_2(Te_{1-x}Se_x)_3$ $(0 < x < 1)$, $(Bi_{1-y}Sb_y)_2Te_3$ $(0 < y < 1)$. *Phys. Status Solidi B* **84**, 619–628 (1977).
35. Ziman, J. M. *Principles of the Theory of Solids* 2nd edn, Ch. 7 (Cambridge Univ. Press, Cambridge, 1979).
36. Gorbachuk, N. P. & Sidorko, V. R. Heat capacity and enthalpy of Bi_2Si_3 and Bi_2Te_3 in the temperature range 58–1012 K. *Powder Metall. Met. Ceramics* **43**, 284–290 (2004).

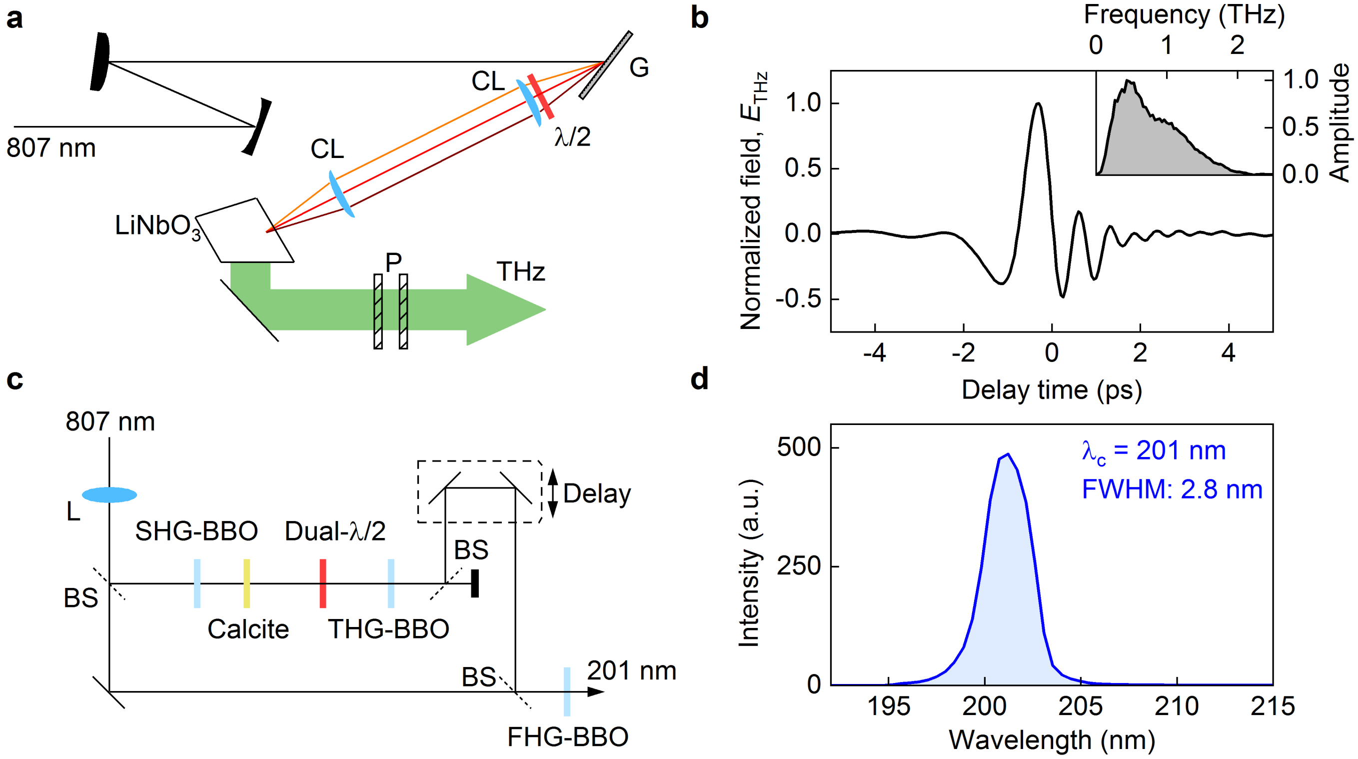

Extended Data Fig. 1 | Optical set-up. a, THz generation via tilted pulse fronts in lithium niobate (LiNbO$_3$). After the laser beam from the titanium:sapphire amplifier system has been reduced in diameter by a reflective telescope, a grating (G) induces a pulse front tilt. Cylindrical lenses (CL) image and focus the beam into a cryogenically cooled LiNbO$_3$ crystal, where optical rectification generates intense THz radiation. A pair of wire-grid polarizers (P) controls the polarization state. **b**, Electro-optically detected THz waveform after transmission through the fused silica window of the vacuum chamber. Inset, amplitude spectrum of the transient shown in **a**. **c**, Set-up for generating UV pulses for photoemission. A lens (L; focal length, 1 m) gently focuses the fundamental titanium:sapphire pulses. A beam splitter (BS) separates 90% of the intensity for second-harmonic generation in a BBO crystal (SHG-BBO). Subsequent dispersion and polarization control is employed using a birefringent calcite plate and a dual-half-wave plate (Dual-λ/2). The third harmonic is generated in another BBO crystal (THG-BBO), separated from the fundamental pulses with a beam splitter (BS), and spatially and temporally (Delay) overlapped with the remaining fundamental pulses to generate the sum-frequency at the fourth harmonic (FHG-BBO). **d**, The resulting spectrum of the fourth harmonic is centred at $\lambda_c = 201$ nm with a full-width at half-maximum (FWHM) of 2.8 nm, corresponding to a Fourier limit of 22 fs.

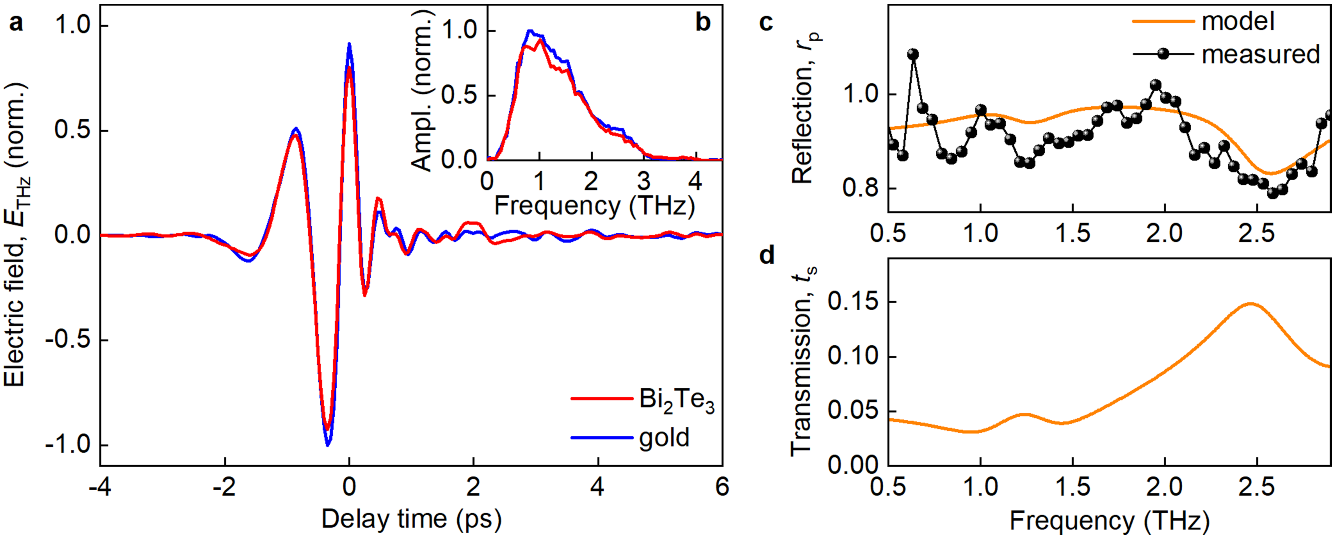

Extended Data Fig. 2 | Determination of the reflectivity of Bi$_2$Te$_3$. **a**, Electro-optically detected THz transients after reflection off a Bi$_2$Te$_3$ (red) and a gold reference (blue) surface kept at a temperature of 77 K. **b**, Amplitude spectra of the field traces in **a** normalized to the amplitude of the gold spectrum. **c**, Reflection coefficient r_p (black spheres) for parallel incidence obtained by dividing the amplitude spectra from Bi$_2$Te$_3$ and gold. The orange curve describes the reflection coefficient r_p calculated using the corresponding Fresnel formula with a Drude–Lorentz model for the dielectric function of Bi$_2$Te$_3$ (see equation (1)). **d**, Transmission coefficient t_s calculated using the modelled dielectric function.

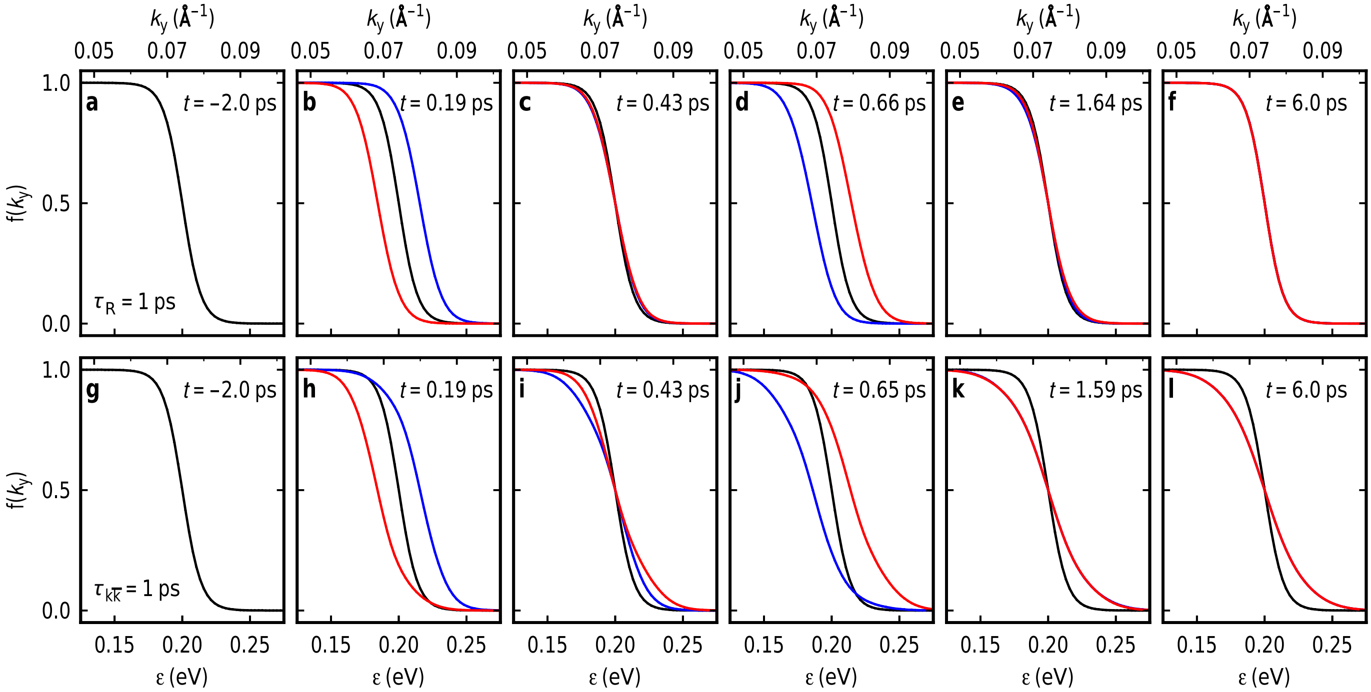

Extended Data Fig. 3 | Comparison of scattering mechanisms. **a**–**l**, Calculated distribution functions at different delay times *t* for the experimental THz waveform with an amplitude of 2.4 kV cm^{-1}. Experimental broadening is not accounted for. The Boltzmann equation used to compute these results includes only the relaxation term (**a**–**f**) or only the effective backscattering term (**g**–**l**).

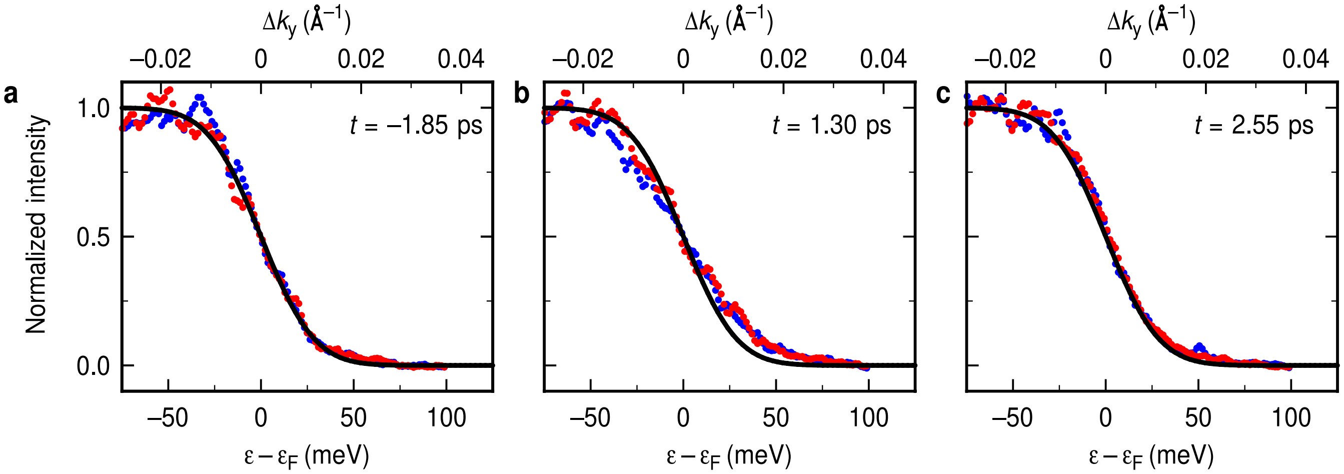

Extended Data Fig. 4 | Broadening of the electron distribution. a–c, Experimental distribution functions (red and blue circles) for different delay times *t* compared to the equilibrium Fermi–Dirac distribution (solid black line).

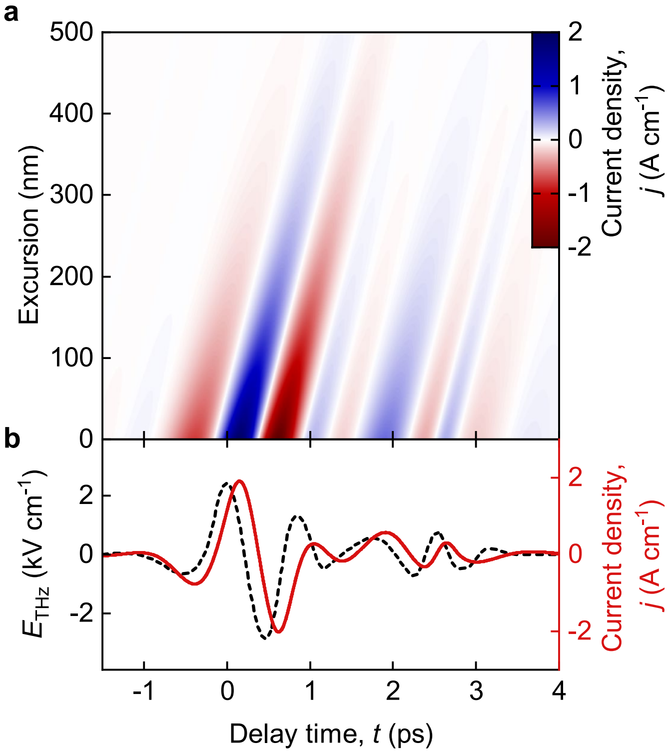

Extended Data Fig. 5 | Local current density in Bi_2Te_3. **a**, Calculated current density j (colour scale) as a function of the delay time t and the electron excursion in the surface layer of Bi_2Te_3. The excursion was evaluated using the extracted scattering times of the charge carriers within the topologically protected surface state. The intense THz fields coherently drive Dirac fermions over several hundred nanometres before they undergo scattering. **b**, The red solid curve shows the simulated current dynamics calculated for scattering times of $\tau_R = \tau_{k\bar{k}} = 1$ ps; the THz electric field is depicted as a dashed black curve.